Supplement of Earth Syst. Sci. Data, 18, 4793–4832, 2026
https://doi.org/10.5194/essd-18-4793-2026-supplement

Open Access Earth System Science Data

Supplement of

A global dataset of δ^{13}C-CH_4 source signatures and associated uncertainties (1998–2022), with a sensitivity analysis to support isotopic inversions

Emeline Tapin et al.

Correspondence to: Emeline Tapin (emeline.tapin@lsce.ipsl.fr)

S1 Additional methods

S1.1 Stable carbon isotope reference scale

All δ^{13}C–CH_4 values reported in this study are expressed relative to the Vienna Pee Dee Belemnite (VPDB) standard, the internationally accepted reference for stable carbon isotope ratios. Historically, earlier atmospheric δ^{13}C–CH_4 simulations used the Pee Dee Belemnite (PDB) reference scale defined by Craig (1957), where $R_{\mathrm{PDB}} = 1.12372 \times 10^{-2}$ is the standard $^{13}C/^{12}C$ ratio. The current VPDB scale adopts a slightly different value, $R_{\mathrm{VPDB}} = 0.011113 \pm 0.000022$ (95% confidence level; Camin et al. 2025).

To assess the consistency between these reference scales, we repeated our model calculations using the updated VPDB standard. The resulting differences in δ^{13}C–CH_4 outputs were negligible, with a mean offset of less than -6e-5‰ over the 24-year simulation period. This confirms that the choice of reference standard does not materially affect the results presented in this work.

S1.2 Method for aggregating isotopic signatures from sub-sectors into sectors

The aggregation of isotopic signatures from sub-sectors into sectoral values was performed using a mass-weighted approach based on the underlying carbon isotopic ratios. When fluxes are provided in mass units rather than moles, appropriate molar mass ratios are applied to ensure consistency. The procedure is as follows:

For each sub-sector i:

1. The isotopic signature $\delta^{13}C_i$ is first converted to the corresponding isotopic ratio R_i relative to the VPDB standard:

   $$R_i = \left(1 + \frac{\delta^{13}\mathrm{C}_i}{1000}\right) R_{\mathrm{PDB}},$$

   where R_{PDB} is the reference $^{13}C/^{12}C$ ratio of the Pee Dee Belemnite (PDB) standard.

2. The partial fluxes of $^{12}CH_4$ and $^{13}CH_4$ for each sub-sector are then calculated as:

   $$F_{12,i} = \frac{F_{\text{total},i}\, M_{^{12}\mathrm{C}}/M_{\mathrm{CH_4}}}{1 + R_i} \qquad F_{13,i} = \frac{F_{\text{total},i}\, R_i\, M_{^{13}\mathrm{C}}/M_{\mathrm{CH_4}}}{1 + R_i},$$

where $F_{\text{total},i}$ is the total methane flux for subcategory i (in mass units), and $M_{^{12}\mathrm{C}}$, $M_{^{13}\mathrm{C}}$ and $M_{\mathrm{CH_4}}$ are the molar masses of ^{12}C, ^{13}C and CH_4, respectively.

3. The fluxes are then summed over all subcategories within a given sector s:

$$F_{12}^s = \sum_i F_{12,i}, \qquad F_{13}^s = \sum_i F_{13,i}.$$

4. The aggregated isotopic ratio for the sector is calculated as:

$$R^s = \frac{F_{13}^s}{F_{12}^s}.$$

5. Finally, the aggregated isotopic signature for the sector is computed as:

$$\delta^{13}\mathrm{C}^s = \left[\frac{R^s}{R_{\mathrm{PDB}}} \frac{M_{^{12}\mathrm{C}}}{M_{^{13}\mathrm{C}}} - 1 \right] \times 1000.$$

This approach ensures that the aggregated isotopic signature is correctly weighted by the contribution of each subsector to the total flux of the sector.

S2 Supplementary tables

S2.1 List of acronyms and datasets used in this study

Table S1. List of acronyms used in this study.

Acronym	Definition / Source
CIF	Community Inversion Framework
VPDB	Vienna Pee Dee Belemnite (standard for stable carbon isotope ratios)
KIE	Kinetic Isotope Effect
FFG	Fossil Fuel exploitation and Geological sources
AGW	Agriculture and Waste
BB	Biomass and Biofuel Burning
WET	Wetlands
NAT	Other Natural Sources
EDGARv8	Emissions Database for Global Atmospheric Research (Crippa et al., 2023)
GFED4s	Global Fire Emissions Database (van Wees et al., 2022)
GMB	Global Methane Budget (Martinez et al., 2024; Saunois et al., 2025)
EMID	European Methane Isotope Database (Menoud et al., 2024)
GFEIv2	Global Fuel Exploitation Inventory (Scarpelli et al., 2022)
CEDSv2021	Community Emissions Data System (O'Rourke et al., 2021)
GAINSv4	Greenhouse Gas and Air Pollution Interactions and Synergies model (Höglund-Isaksson et al., 2020)
RSD	Relative Standard Deviation
SD	Standard Deviation

S2.2 European fossil-fuels isotopic signature aggregation

Table S2. Country-level weighted mean δ^{13}C-CH_4 values (‰) for oil & gas and coal emissions in Europe, derived from data compiled by Lan et al. (2021) and Menoud et al. (2022). N indicates the number of individual measurements contributing to each dataset. A weighted mean is calculated when data from both sources are available.

Country	δ^{13}C-CH_4 (Lan et al., 2021) (‰) / N	δ^{13}C-CH_4 (Menoud et al., 2022) (‰) / N	Weighted mean (‰)
Oil & Gas			
France	-44.0 / 28	-44.8 / 30	-44.4
United Kingdom	-39.2 / 13	-40.2 / 135	-40.1
Germany	-43.8 / 176	-39.3 / 29	-43.2
Poland	-47.0 / 57	-44.9 / 27	-46.3
Romania	-48.3 / –	-37.7 / 143	-37.7
Netherlands	–	-44.8 / 11	-44.8
Coal			
United Kingdom	-40.1 / 23	-48.8 / 4	-41.2
Germany	-43.1 / 90	-44.7 / 3	-43.2
Poland	-49.5 / 64	-49.2 / 64	-49.4

S2.3 Monte Carlo ensemble simulations of isotopic source signatures

Table S3. Parameters used for the Monte Carlo ensemble simulations of isotopic source signatures. For each of the five main source sectors, normal distributions were defined based on literature-derived mean and standard deviation values (see Section 4.1.3). Five ensemble members were drawn per sector to represent the uncertainty in $\delta^{13}CH_4$ source signatures. The table includes sector-specific mean isotopic signatures and their variability, with spatial granularity used for Monte Carlo: 110 countries (Natural Earth dataset, free vector and raster map data at naturalearthdata.com) for anthropogenic sectors (FFG, AGW) reflecting country-level variability, and 18 GCP regions (Saunois et al., 2020) for natural sectors (BB, WET, NAT) reflecting coarser regional variability.

Sector	Mean signature [‰]	Standard deviation (1σ) [%]	Spatial granularity
Fossil Fuel & Geological (FFG)	-44.2	13.9	110 countries
Agriculture and Waste (AGW)	-60.2	5.5	110 countries
Biomass & Biofuel Burning (BB)	-24.3	24.9	18 GCP regions
Wetlands (WET)	-58.6	12.8	18 GCP regions
Other Natural (NAT)	-51.9	10.4	18 GCP regions

S3 Supplementary figures

S3.1 Detailed sub-sectors δ^{13}C-CH_4 source signature maps

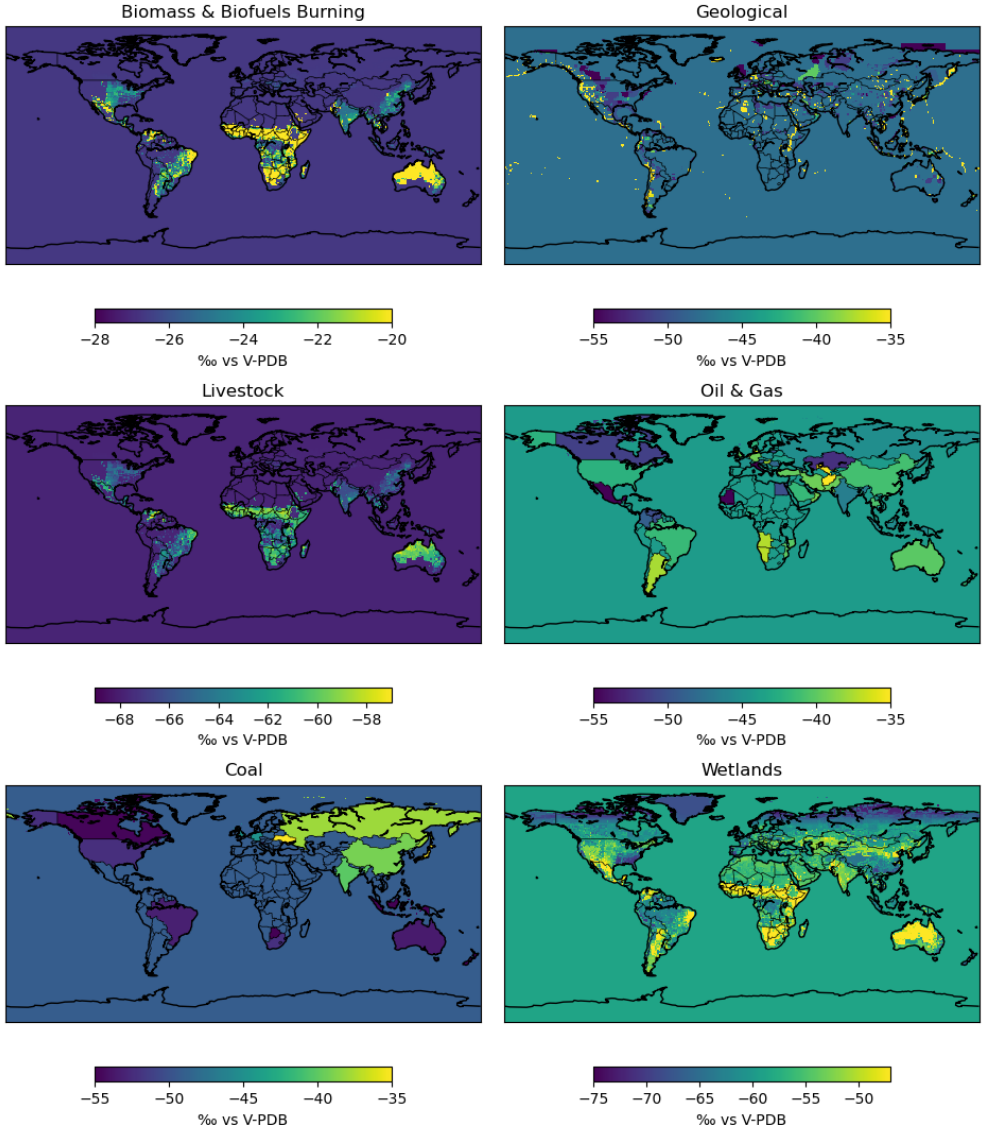

Figure S1. Maps of δ^{13}C-CH_4 subcategories, showing isotopic signatures by source subcategory. Sources for sector isotopic signatures are: Biomass – Biofuels Burning (Lan et al., 2021), Geological (Etiope et al., 2019), Livestock (Lan et al., 2021), Oil and Gas (Lan et al., 2021; Menoud et al., 2022), Coal (Lan et al., 2021; Menoud et al., 2022), and Wetlands (Oh et al., 2022).

S3.2 Detailed sub-sectors CH_4 emissions maps

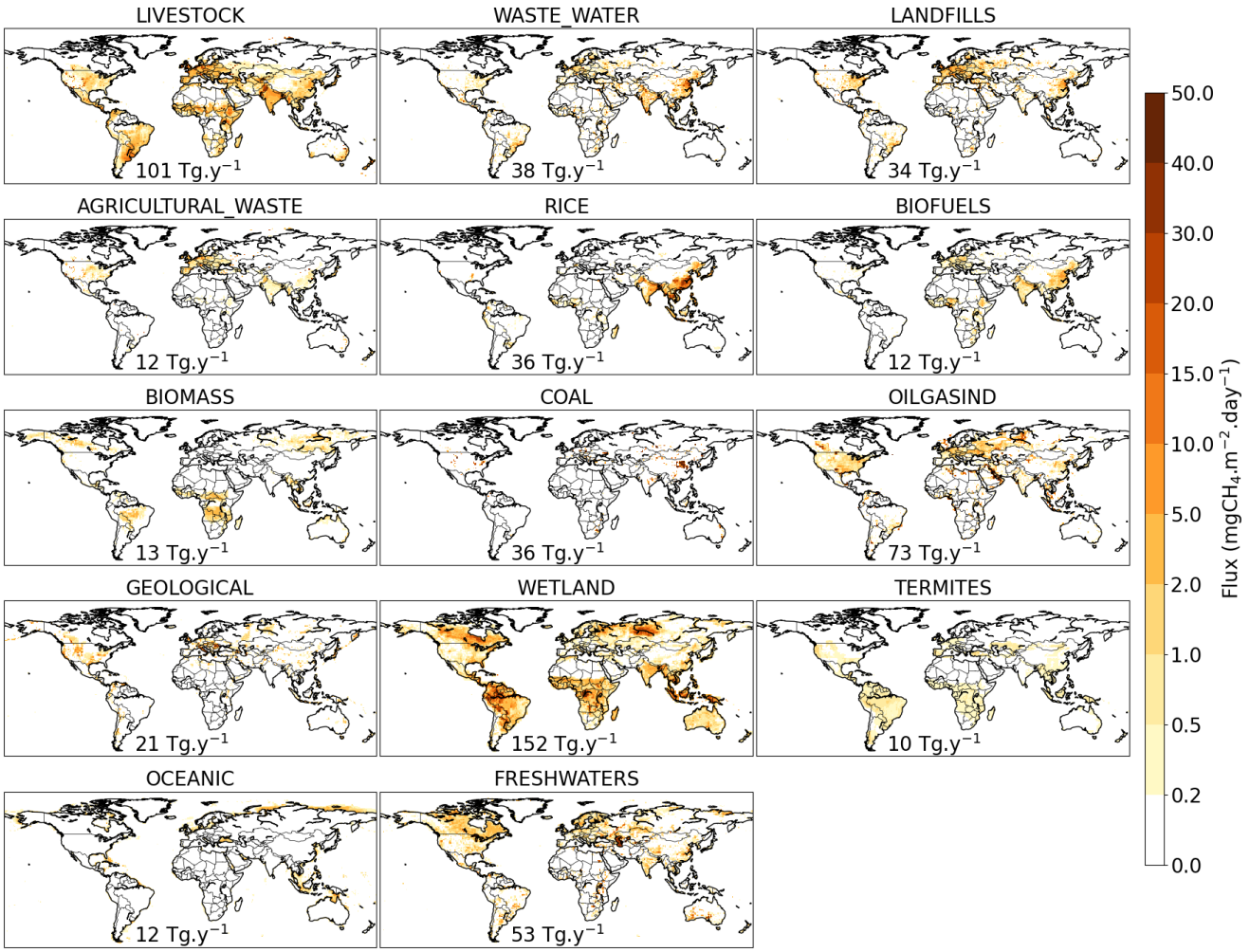

Figure S2. Mean methane emissions (1998–2022) for each sub-sector contributing to the five main CH_4 source sectors, expressed in mgCH_4 m^{-2} day^{-1}. Each panel shows the spatial distribution of the average flux over the 1998–2022 period, with the total subcategory emission (in Tg yr^{-1}) indicated. Anthropogenic emissions (e.g., RICE, LANDFILLS, LIVESTOCK, WASTEWATER, AGRICULTURAL WASTE, BIOFUELS, COAL, OIL AND GAS) are from EDGARv8.0 (Crippa et al., 2023). Biomass burning emissions (BIOMASS) are derived from GFED4s (van Wees et al., 2022). Wetland emissions correspond to the climatological mean of 11 process-based models from the Global Methane Budget (GMB) (Martinez et al., 2024). Freshwater emissions are based on CH_4 flux maps from Stavert et al. (2022), with spatial rescaling following Martinez et al. (2024). Geological, termite, and oceanic emissions follow the GMB prior dataset, based respectively on Etiope et al. (2019), the S. Castaldi model for termites (Martinez et al., 2024), and oceanic emissions from Weber et al. (2019). All datasets were harmonised to a common $1^\circ \times 1^\circ$ grid.

S3.3 Sensitivity analysis

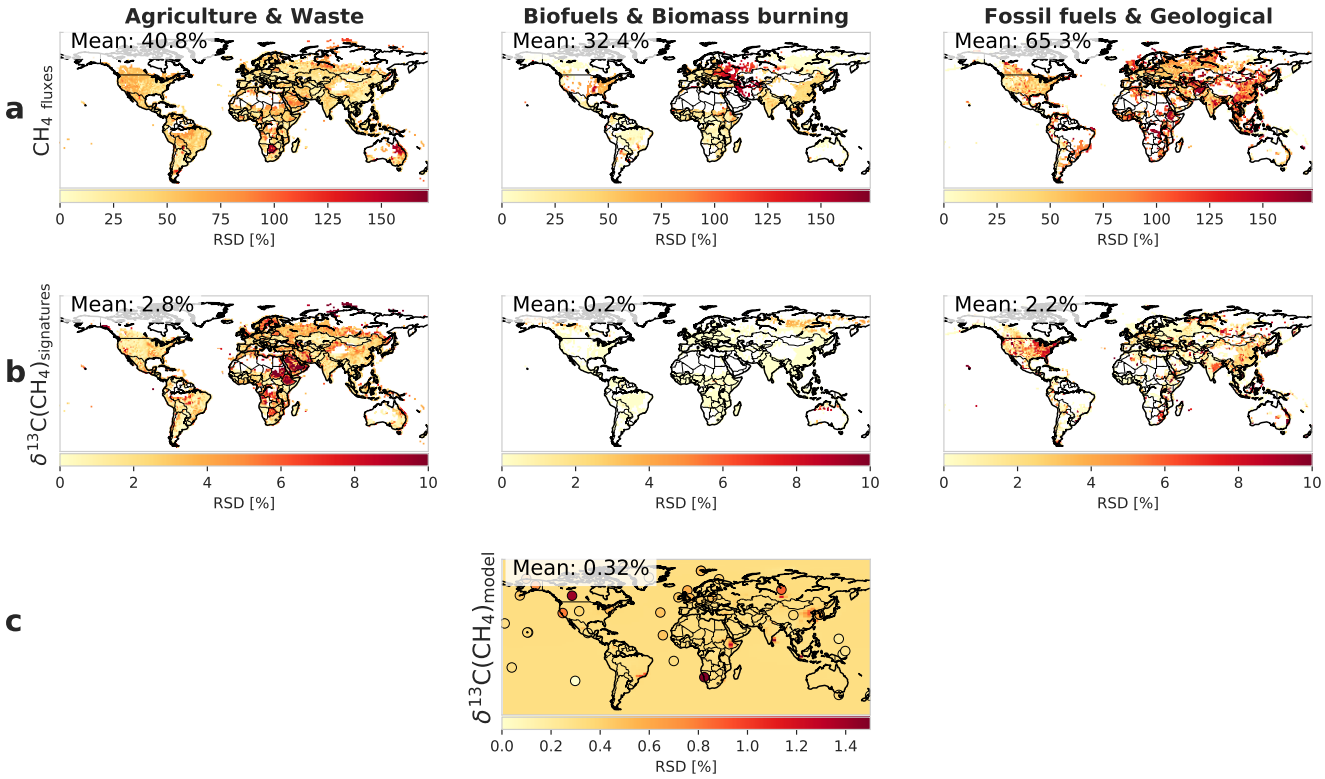

Figure S3. (a) RSD (in %) of the fluxes among different prior datasets (GAINSv4, CEDSv2021, GFEIv2, EDGARv8) (over 2016–2020) at surface level. Values are only displayed when the associated CH_4 flux is higher than 0.2 $mgCH_4 \cdot m^{-2} \cdot day^{-1}$, for aggregated categories. (b) RSD of the resulting δ^{13}C-CH_4 source signature by aggregated category. (c) RSD of the δ^{13}C-CH_4 signals from the forward model outputs at surface level. Coloured circles indicate RSD of observed δ^{13}C-CH_4 values at each surface station over the study period.

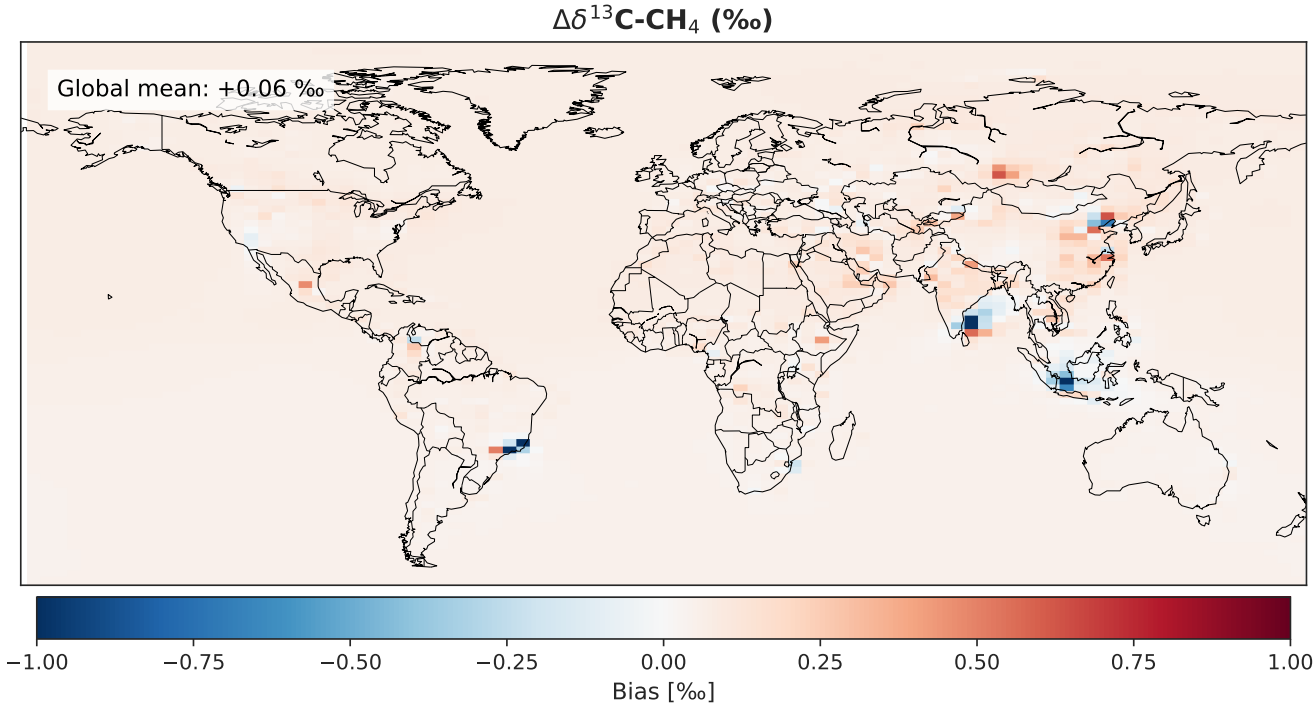

Figure S4. Difference maps between the NO_AGGREG (14 categories) and the reference OH_INCA simulation (5 categories) averaged over 2016–2020 at the surface level for $\Delta\delta^{13}$C-CH$_4$ (‰).

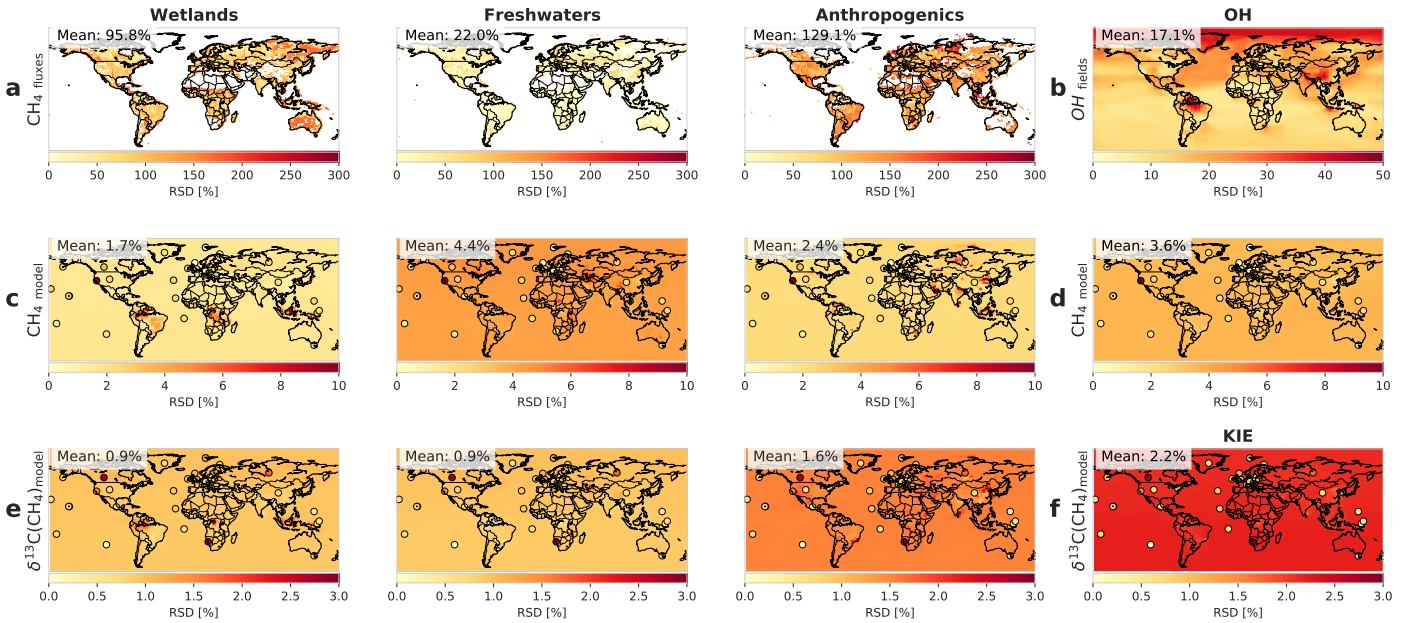

Figure S5. RSD (in %) over 2016–2020 at surface level. (a) RSD of CH_4 emissions from wetlands, freshwaters, and anthropogenic sectors (AGW, FFG, BB). Values are only displayed when the associated CH_4 flux exceeds 0.2 mg $CH_4 \cdot m^{-2} \cdot day^{-1}$. (b) RSD of the total tropospheric OH column (pressure levels below 250 hPa). (c) RSD of CH_4 mole fractions at surface level from forward model outputs, driven by uncertainty in emission fluxes. Coloured circles indicate RSD of observed CH_4 mole fractions at surface stations with co-located $\delta^{13}C(CH_4)$ measurements. (d) Same as (c), but driven by uncertainty in OH fields. (e) RSD of $\delta^{13}C$-CH_4 values at surface level from forward model outputs, driven by uncertainty in emission fluxes. Coloured circles indicate RSD of observed $\delta^{13}C$-CH_4 values at the same stations. (f) Same as (e), but driven by uncertainty in kinetic isotope effects (KIE) during CH_4 oxidation.

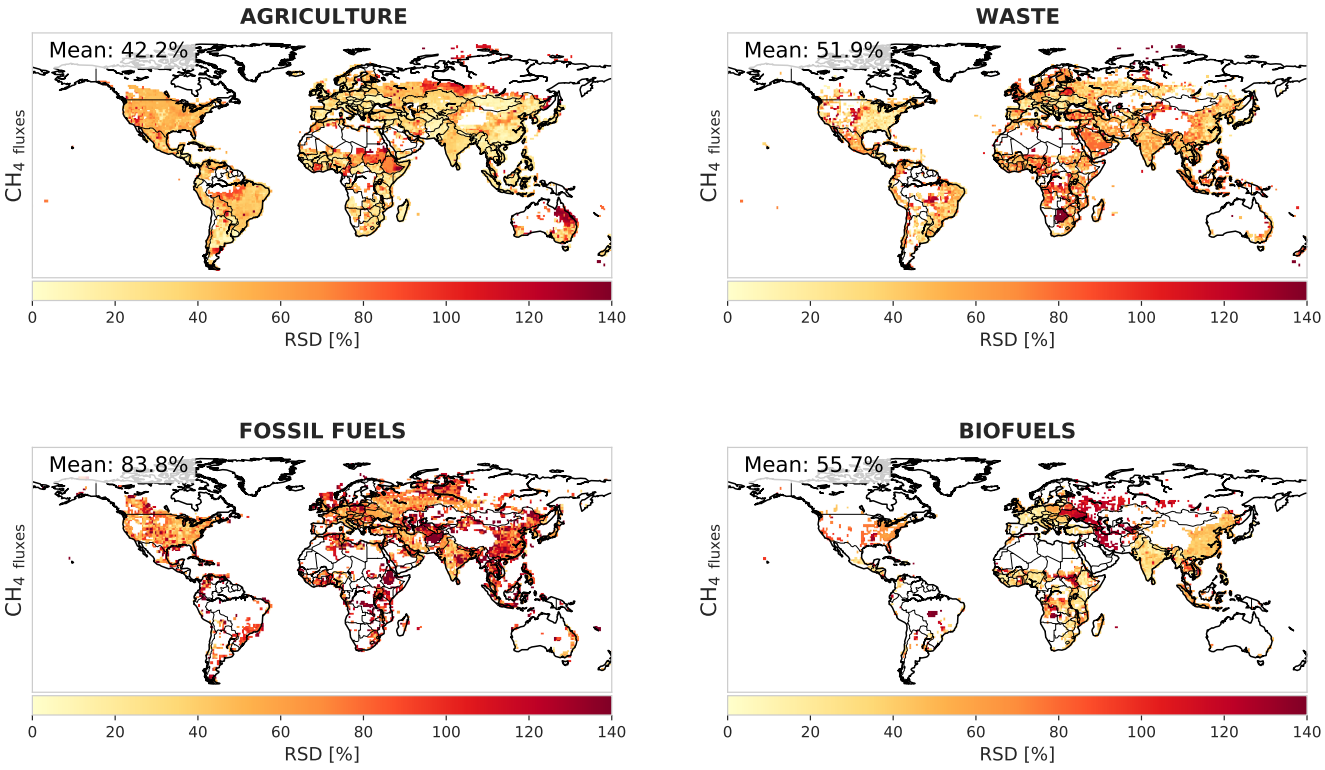

Figure S6. RSD (in %) of fluxes included in anthropogenics sector of annual mean CH_4 fluxes across four inventories (EDGARv8, CEDS, GAINS, GFEI) over (over 2016–2020), shown by emission sub-sector. Values are only displayed when the associated CH_4 flux is higher than 0.2 $mgCH_4 \cdot m^{-2} \cdot day^{-1}$

Sub-sector grouping used in this figure:

AGRICULTURE: LIVESTOCK, RICE

WASTE: AGRICULTURAL_WASTE, LANDFILLS, WASTE_WATER

FOSSIL FUELS: COAL, OILGASIND

BIOFUELS: BIOFUELS

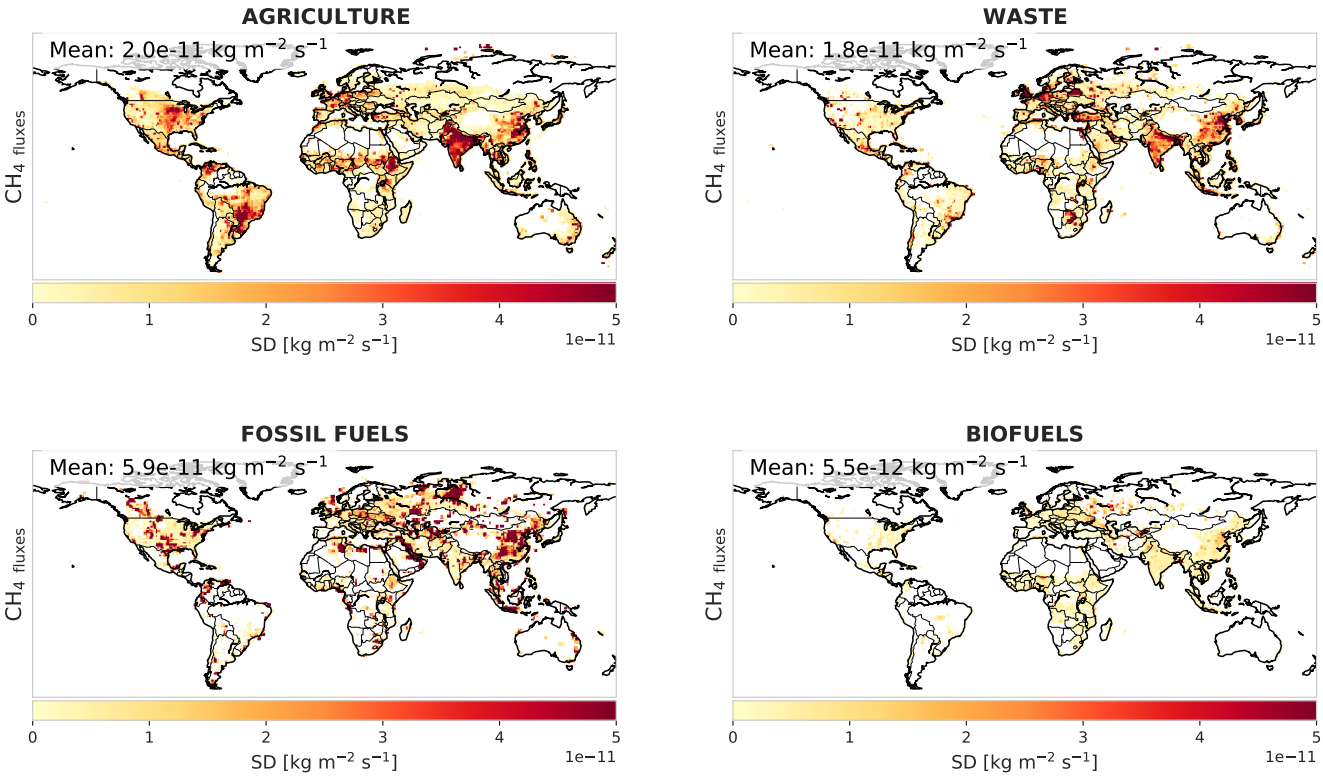

Figure S7. SD (in kg .m^{-2} .s^{-1}) of fluxes included in the anthropogenic sector of annual mean CH_4 fluxes across four inventories (EDGARv8, CEDS, GAINS, GFEI) over 2016–2020, shown by emission sub-sector. Values are only displayed when the associated CH_4 flux is higher than 0.2 mgCH_4·m^{-2}·day^{-1}.

Sub-sector grouping used in this figure:

AGRICULTURE: LIVESTOCK, RICE

WASTE: AGRICULTURAL_WASTE, LANDFILLS, WASTE_WATER

FOSSIL FUELS: COAL, OILGASIND

BIOFUELS: BIOFUELS

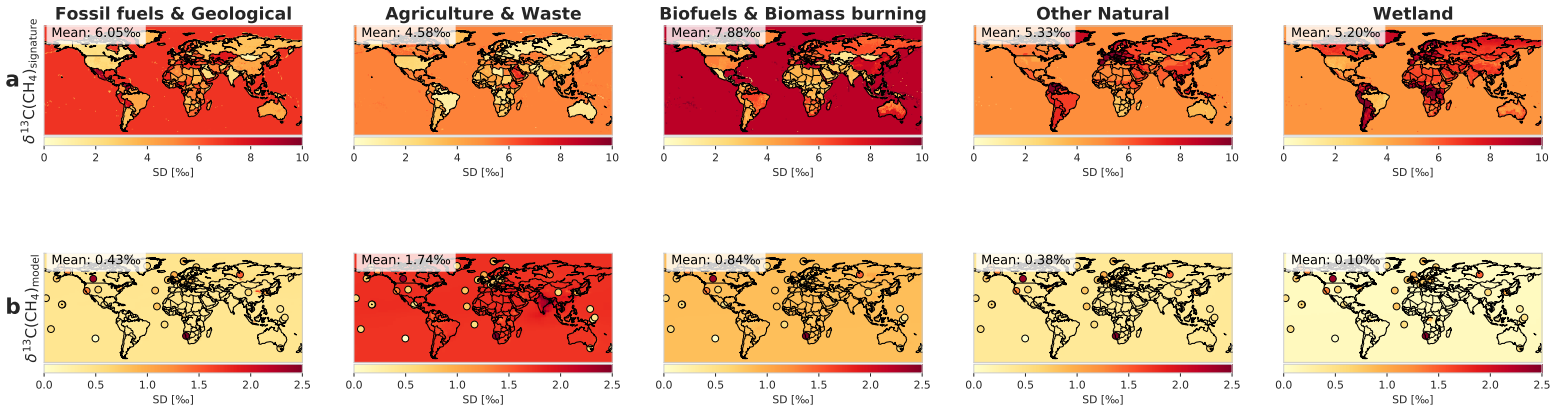

Figure S8. (a) RSD (in %) of the δ^{13}C-CH_4 source signature sensitivities inputs for Monte Carlo simulations, by sector, at surface level. (b) RSD of the δ^{13}C-CH_4 source signal from Monte Carlo simulations, by sector, at surface level. Coloured circles indicate RSD of observed δ^{13}C-CH_4 values at each surface station over the study period.

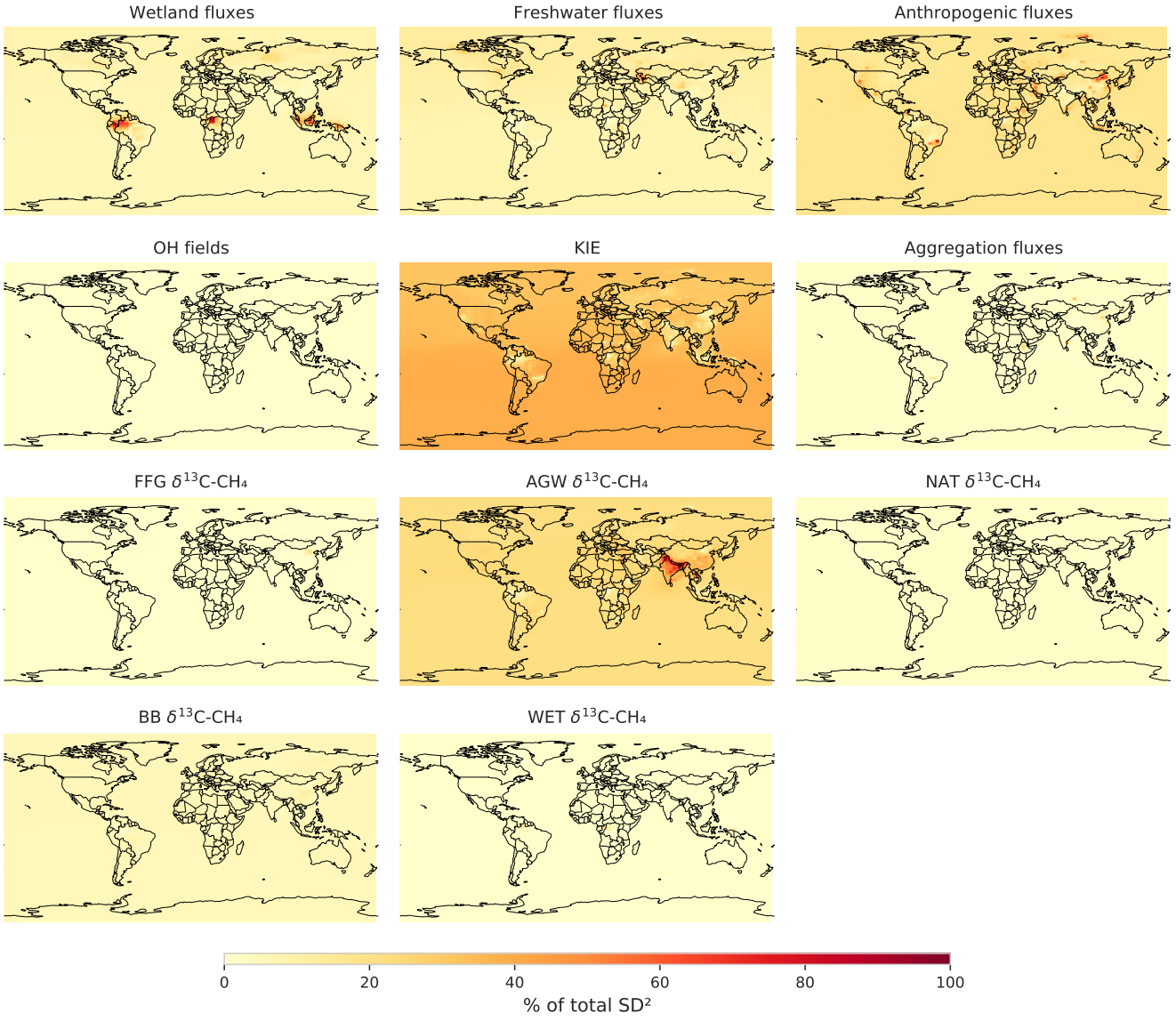

Figure S9. Relative contribution (in %) of each parameter to the total variance of simulated atmospheric δ^{13}C-CH$_4$ at each model grid cell. Each panel represents one sensitivity parameter tested. Colors indicate the percentage contribution of the squared standard deviation of each parameter to the total variance across all parameters. Values are calculated independently at each grid cell.

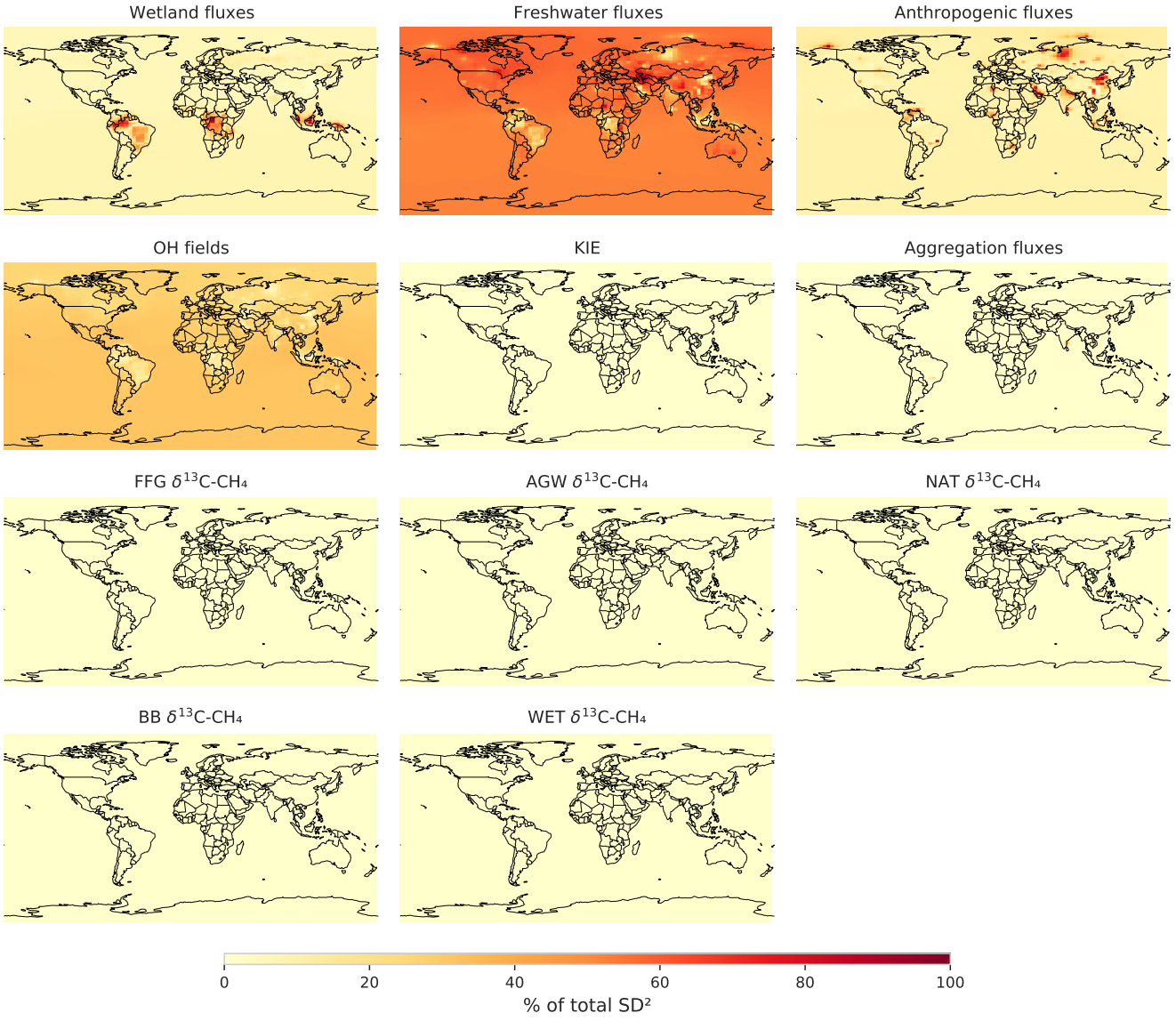

Figure S10. Relative contribution (in %) of each parameter to the total variance of simulated atmospheric CH_4 at each model grid cell. Each panel represents one sensitivity parameter tested. Colors indicate the percentage contribution of the squared standard deviation of each parameter to the total variance across all parameters. Values are calculated independently at each grid cell.

S4 Model-observation comparison

S4.1 Globally averaged time series of the sensitivity simulations

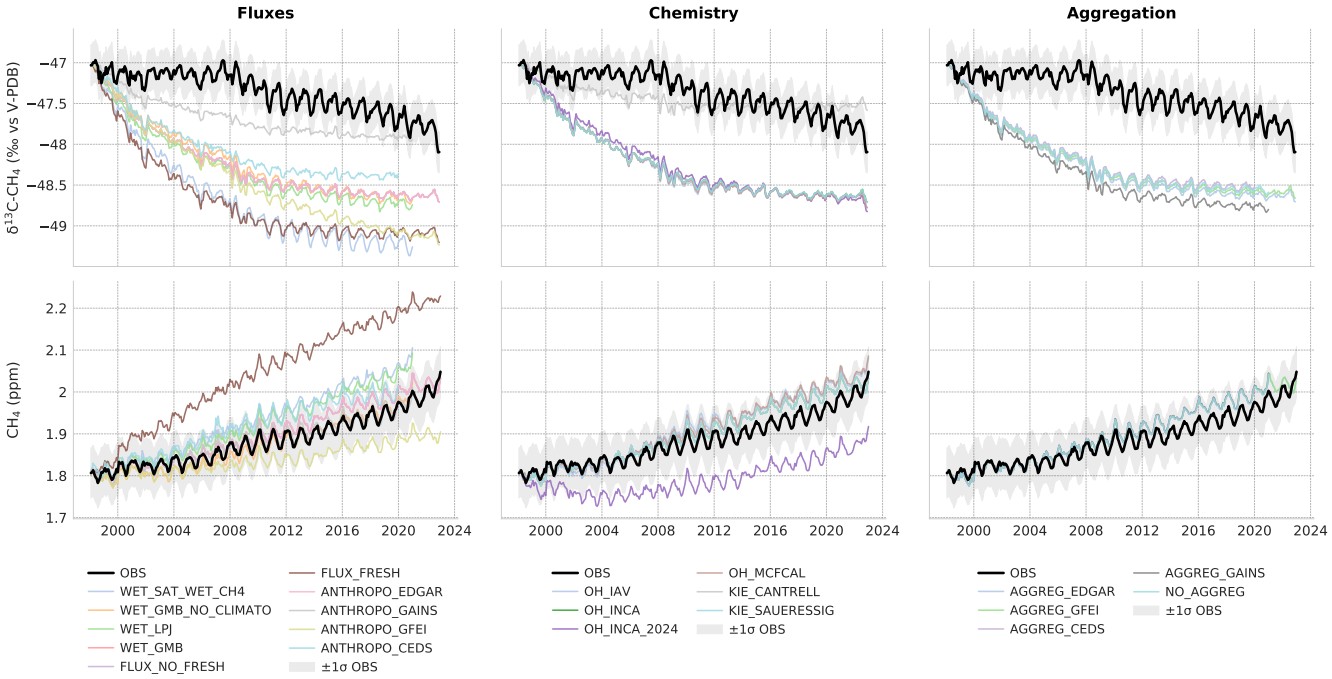

Figure S11. Globally averaged surface time series (1998–2022) of δ^{13}C-CH_4 signal (top row, ‰ vs V-PDB) and CH_4 mole fraction (bottom row, ppm) for all forward sensitivity simulations described in Table 3 of the main text, grouped by perturbation category: Fluxes (left), Chemistry (middle) and Aggregation (right). Black solid line: NOAA-INSTAAR globally averaged observations (Michel et al., 2024; Schuldt et al., 2025); grey shading: $\pm 1\sigma$ observational uncertainty. Coloured lines correspond to the individual simulations (see legends for configuration details). Simulations based on GAINS and GFEI inventories end in 2020 due to data availability.

Figure S11 presents the globally averaged surface time series (1998–2022) of CH_4 mole fractions (bottom row) and δ^{13}C-CH_4 signals (top row) for all forward sensitivity simulations listed in Table 3 of the main text, grouped by perturbation category: Fluxes (left column), Chemistry (middle column), and Aggregation (right column). The black solid line shows the NOAA-INSTAAR globally averaged observations (Michel et al., 2024; Schuldt et al., 2025), and the grey shaded envelope represents the $\pm 1\sigma$ observational uncertainty. Observations are provided here as a plausibility reference rather than a validation target: the simulations use prescribed fluxes and source signatures rather than posterior estimates from an inversion.

The inter-simulation spread is category-dependent. Aggregation simulations cluster tightly around a common trajectory for both CH_4 and δ^{13}C-CH_4, consistent with the limited impact of aggregation choices reported in Sect. 4.2.1 of the main text. Chemistry simulations split into two groups in δ^{13}C-CH_4: the KIE_CANTRELL run remains systematically enriched compared to the KIE_SAUERESSIG, consistent with the dominant sensitivity of the modeled isotopic signal to the OH-KIE

value (Table 6 of the main text); the OH_INCA_2024 run departs from the other OH configurations in CH_4, reflecting the higher prescribed OH concentrations. Flux simulations display the widest spread overall, in particular ANTHROPO_GFEI progressively diverging upward in CH_4 after 2008.

Most simulations remain within the observational envelope over the full period, supporting the realism of the prescribed input datasets for mainstream configurations. The outlier behaviour of KIE_CANTRELL, OH_INCA_2024 and ANTHROPO_GFEI illustrates that individual parameter choices, rather than the overall modeling framework, drive discrepancies with observations. The inter-simulation spread nonetheless reaches $\sim$1.5 ‰ in δ^{13}C-CH_4 and $\sim$300 ppb in CH_4 by the end of the period, confirming that forward simulations alone cannot reproduce observations without joint optimization of fluxes and isotopic source signatures within an inversion framework.

The model–observation offset is largest during the early simulation period and progressively stabilizes after approximately 2010–2015. This spin-up drift, particularly visible in δ^{13}C-CH_4 (Tans, 1997), and confirms that restricting the sensitivity analysis to the 2016–2020 window ensures a stationary regime across all simulations, isolating the effect of perturbed parameters from residual spin-up artifacts.

S4.2 Inter-hemispheric gradient diagnostic

As a complementary first-order diagnostic of the realism of the modeled fields, Figure S12 compares the inter-hemispheric gradient (NH–SH, computed as the difference between the latitudinally averaged Northern and Southern Hemisphere surface signals) for both CH_4 and δ^{13}C-CH_4, averaged over the analysis window 2016–2019. The inter-hemispheric gradient is a particularly stringent test as it isolates the joint contribution of the spatial distribution of sources, inter-hemispheric transport and oxidation chemistry, while being insensitive to absolute calibration offsets and to long-term spin-up drift. NOAA-INSTAAR observations (Michel et al., 2024; Schuldt et al., 2025) are processed identically to the simulations, using the same set of surface stations.

For CH_4, the observed gradient ($\sim$0.117 ppb) falls well within the spread of simulations (0.10–0.14 ppb). The reference configuration (OH_INCA / KIE_SAUERESSIG / EDGAR / GMB_Mean) reproduces the observed value to within $\sim$5 %, supporting the realism of the prescribed flux distribution at hemispheric scale. The strongest deviations are found for ANTHROPO_GFEI (low gradient, consistent with its underestimated NH emissions) and FLUX_FRESH (higher gradient, reflecting the addition of freshwater fluxes predominantly located in the Northern Hemisphere).

For δ^{13}C-CH_4, all simulations systematically underestimate the magnitude of the observed gradient (-0.32 ‰ observed vs. -0.15 to -0.25 ‰ simulated). This residual bias is fully consistent with the dominant uncertainty drivers identified in our sensitivity analysis: the OH kinetic isotope effect and the agriculture and waste source signatures (Sect. 4.3.1 of the main text), which jointly control the partitioning of ^{13}C between the two hemispheres. The ranking of simulations also matches expectations: WET_GMB_NO_CLIMATO and WET_SAT_WET_CH4 produce the most negative gradients (closest to observations) thanks to a stronger seasonal contribution from boreal wetlands, while the NO_AGGREG, AGGREG_GFEI and ANTHROPO_EDGAR runs produce the weakest gradients. This residual bias does not undermine the realism of the dataset, but rather reinforces the methodological recommendations formulated in Sect. 4.3.2: in isotopic inversions, OH-KIE and AGW

source signatures must be either explicitly optimized or sampled within an ensemble framework, since their prescribed values drive a systematic structural bias in the modeled inter-hemispheric isotopic gradient.

We emphasize that this diagnostic is a plausibility reference rather than a formal validation. Forward simulations alone cannot disentangle biases on fluxes from biases on isotopic source signatures, and only joint optimization within an inversion framework would allow rigorous validation. The diagnostics provided in Figures S11 and S12 therefore demonstrate that the dataset produces a realistic mean state and inter-hemispheric structure for CH_4, while explicitly identifying where the remaining work is needed for δ^{13}C-CH_4. Inversion-based validation will be the subject of a follow-up study.

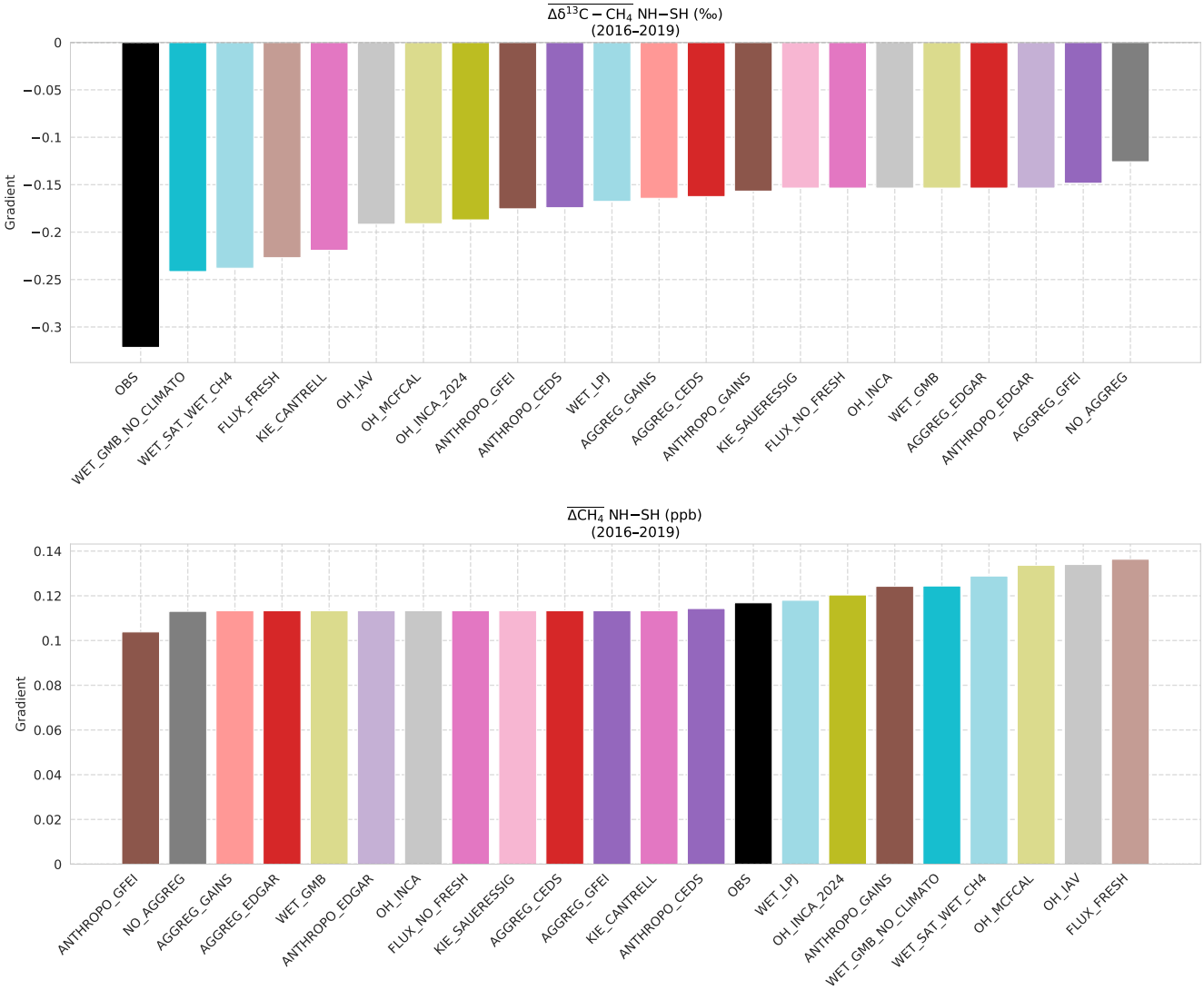

Figure S12. Inter-hemispheric gradient (NH–SH) of δ^{13}C-CH_4 (top, ‰ vs V-PDB) and CH_4 (bottom, ppb) averaged over 2016–2019, for all forward sensitivity simulations described in Table 3 of the main text and for NOAA-INSTAAR observations (Michel et al., 2024; Schuldt et al., 2025) (black bar). Simulations are sorted by increasing gradient. The NH–SH gradient is computed from monthly surface fields, taking the difference between the latitudinally averaged Northern Hemisphere (0°–90°N) and Southern Hemisphere (90°S–0°) signals at the locations of NOAA-INSTAAR surface stations, and then averaged over 2016–2019.

References

Camin, F., Besic, D., Brewer, P. J., Allison, C. E., Coplen, T. B., Dunn, P. J. H., Gehre, M., Gröning, M., Meijer, H. A. J., Hélie, J.-F., Iacumin, P., Kraft, R., Krajnc, B., Kümmel, S., Lee, S., Meija, J., Mester, Z., Mohn, J., Moossen, H., Qi, H., Skrzypek, G., Sperlich, P., Viallon, J., Wassenaar, L. I., and Wielgosz, R. I.: Stable Isotope Reference Materials and Scale Definitions—Outcomes of the 2024 IAEA Experts Meeting, Rapid Communications in Mass Spectrometry, 39, e10 018, https://doi.org/10.1002/rcm.10018, 2025.

Craig, H.: Isotopic Standards for Carbon and Oxygen and Correction Factors for Mass-Spectrometric Analysis of Carbon Dioxide, Geochimica et Cosmochimica Acta, 12, 133–149, https://doi.org/10.1016/0016-7037(57)90024-8, 1957.

Crippa, M., Guizzardi, D., Schaaf, E., Monforti-Ferrario, F., Quadrelli, R., Risquez Martin, A., Rossi, S., Vignati, E., Muntean, M., Brandao De Melo, J., Oom, D., Pagani, F., Banja, M., Taghavi-Moharamli, P., Köykkä, J., Grassi, G., Branco, A., and San-Miguel, J.: GHG Emissions of All World Countries: 2023, Publications Office of the European Union, ISBN 978-92-68-07550-0, 2023.

Etiope, G., Ciotoli, G., Schwietzke, S., and Schoell, M.: Gridded Maps of Geological Methane Emissions and Their Isotopic Signature, Earth System Science Data, 11, 1–22, https://doi.org/10.5194/essd-11-1-2019, 2019.

Höglund-Isaksson, L., Gómez-Sanabria, A., Klimont, Z., Rafaj, P., and Schöpp, W.: Technical Potentials and Costs for Reducing Global Anthropogenic Methane Emissions in the 2050 Timeframe –Results from the GAINS Model, Environmental Research Communications, 2, 025 004, https://doi.org/10.1088/2515-7620/ab7457, 2020.

Lan, X., Basu, S., Schwietzke, S., Bruhwiler, L. M. P., Dlugokencky, E. J., Michel, S. E., Sherwood, O. A., Tans, P. P., Thoning, K., Etiope, G., Zhuang, Q., Liu, L., Oh, Y., Miller, J. B., Pétron, G., Vaughn, B. H., and Crippa, M.: Improved Constraints on Global Methane Emissions and Sinks Using δ13C-CH4, Global Biogeochemical Cycles, 35, e2021GB007 000, https://doi.org/10.1029/2021GB007000, 2021.

Martinez, A., Saunois, M., Poulter, B., Bousquet, P., Canadell, J. G., Jackson, R. B., Dlugokencky, E. J., Ciais, P., Bastviken, D., Blake, D. R., Castaldi, S., Etiope, G., Gedney, N., Höglund-Isaksson, L., Hugelius, G., Ito, A., Kleinen, T., Krummel, P. B., Liu, L., McDonald, K. C., Melton, J. R., Müller, J., Murguia-Flores, F., Niwa, Y., Noce, S., Parker, R. J., Peng, C., Ramonet, M., Riley, W. J., Rosentreter, J. A., Segers, A., Smith, S. J., Tian, H., Tubiello, F. N., Tsuruta, A., Weber, T. S., van der Werf, G. R., Worthy, D., Yoshida, Y., Zhang, W., Zhang, Z., Zheng, B., Zhu, Q., Zhu, Q., and Zhuang, Q.: Supplemental Data of the Global Carbon Project Methane Budget 2024 V1, https://doi.org/10.18160/GKQ9-2RHT, 2024.

Menoud, M., van der Veen, C., Lowry, D., Fernandez, J. M., Bakkaloglu, S., France, J. L., Fisher, R. E., Maazallahi, H., Stanisavljević, M., Nęcki, J., Vinkovic, K., Łakomiec, P., Rinne, J., Korbeń, P., Schmidt, M., Defratyka, S., Yver-Kwok, C., Andersen, T., Chen, H., and Röckmann, T.: New Contributions of Measurements in Europe to the Global Inventory of the Stable Isotopic Composition of Methane, Earth System Science Data, 14, 4365–4386, https://doi.org/10.5194/essd-14-4365-2022, 2022.

Menoud, M., Thomas, R., Carina, v. d. V., Julianne, F., Semra, B., Dave, L., James, F., Rebecca, F., Hossein, M., Piotr, K., Martina, S., Mila, S., Jaroslaw, N., Patryk, Ł., Janne, R., Sara, D., Camille, Y.-K., Katarina, V., Truls, A., and Huilin, C.: The European Methane Isotope Database Coupled with a Global Inventory of Fossil and Non-Fossil δ13C- and δ2H-CH4 Source Signature Measurements, https://doi.org/10.24416/UU01-YP43IN, 2024.

Michel, S. E., Lan, X., Miller, J., Tans, P., Clark, J. R., Schaefer, H., Sperlich, P., Brailsford, G., Morimoto, S., Moossen, H., and Li, J.: Rapid Shift in Methane Carbon Isotopes Suggests Microbial Emissions Drove Record High Atmospheric Methane Growth in 2020–2022, Proceedings of the National Academy of Sciences, 121, e2411212 121, https://doi.org/10.1073/pnas.2411212121, 2024.

Oh, Y., Zhuang, Q., Welp, L. R., Liu, L., Lan, X., Basu, S., Dlugokencky, E. J., Bruhwiler, L., Miller, J. B., Michel, S. E., Schwietzke, S., Tans, P., Ciais, P., and Chanton, J. P.: Improved Global Wetland Carbon Isotopic Signatures Support Post-2006 Microbial Methane Emission Increase, Communications Earth & Environment, 3, 1–12, https://doi.org/10.1038/s43247-022-00488-5, 2022.

O'Rourke, P., Smith, S., Mott, A., Ahsan, H., Mcduffie, E., Crippa, M., Klimont, Z., Mcdonald, B., Wang, S., Nicholson, M., Hoesly, R., and Feng, L.: CEDS V_2021_04_21 Gridded Emissions Data, https://doi.org/10.25584/PNNLDATAHUB/1779095, 2021.

Saunois, M., Stavert, A. R., Poulter, B., Bousquet, P., Canadell, J. G., Jackson, R. B., Raymond, P. A., Dlugokencky, E. J., Houweling, S., Patra, P. K., Ciais, P., Arora, V. K., Bastviken, D., Bergamaschi, P., Blake, D. R., Brailsford, G., Bruhwiler, L., Carlson, K. M., Carrol, M., Castaldi, S., Chandra, N., Crevoisier, C., Crill, P. M., Covey, K., Curry, C. L., Etiope, G., Frankenberg, C., Gedney, N., Hegglin, M. I., Höglund-Isaksson, L., Hugelius, G., Ishizawa, M., Ito, A., Janssens-Maenhout, G., Jensen, K. M., Joos, F., Kleinen, T., Krummel, P. B., Langenfelds, R. L., Laruelle, G. G., Liu, L., Machida, T., Maksyutov, S., McDonald, K. C., McNorton, J., Miller, P. A., Melton, J. R., Morino, I., Müller, J., Murguia-Flores, F., Naik, V., Niwa, Y., Noce, S., O'Doherty, S., Parker, R. J., Peng, C., Peng, S., Peters, G. P., Prigent, C., Prinn, R., Ramonet, M., Regnier, P., Riley, W. J., Rosentreter, J. A., Segers, A., Simpson, I. J., Shi, H., Smith, S. J., Steele, L. P., Thornton, B. F., Tian, H., Tohjima, Y., Tubiello, F. N., Tsuruta, A., Viovy, N., Voulgarakis, A., Weber, T. S., van Weele, M., van der Werf, G. R., Weiss, R. F., Worthy, D., Wunch, D., Yin, Y., Yoshida, Y., Zhang, W., Zhang, Z., Zhao, Y., Zheng, B., Zhu, Q., Zhu, Q., and Zhuang, Q.: The Global Methane Budget 2000–2017, Earth System Science Data, 12, 1561–1623, https://doi.org/10.5194/essd-12-1561-2020, 2020.

Saunois, M., Martinez, A., Poulter, B., Zhang, Z., Raymond, P. A., Regnier, P., Canadell, J. G., Jackson, R. B., Patra, P. K., Bousquet, P., Ciais, P., Dlugokencky, E. J., Lan, X., Allen, G. H., Bastviken, D., Beerling, D. J., Belikov, D. A., Blake, D. R., Castaldi, S., Crippa, M., Deemer, B. R., Dennison, F., Etiope, G., Gedney, N., Höglund-Isaksson, L., Holgerson, M. A., Hopcroft, P. O., Hugelius, G., Ito, A., Jain, A. K., Janardanan, R., Johnson, M. S., Kleinen, T., Krummel, P. B., Lauerwald, R., Li, T., Liu, X., McDonald, K. C., Melton, J. R., Mühle, J., Müller, J., Murguia-Flores, F., Niwa, Y., Noce, S., Pan, S., Parker, R. J., Peng, C., Ramonet, M., Riley, W. J., Rocher-Ros, G., Rosentreter, J. A., Sasakawa, M., Segers, A., Smith, S. J., Stanley, E. H., Thanwerdas, J., Tian, H., Tsuruta, A., Tubiello, F. N., Weber, T. S., van der Werf, G. R., Worthy, D. E. J., Xi, Y., Yoshida, Y., Zhang, W., Zheng, B., Zhu, Q., Zhu, Q., and Zhuang, Q.: Global Methane Budget 2000–2020, Earth System Science Data, 17, 1873–1958, https://doi.org/10.5194/essd-17-1873-2025, 2025.

Scarpelli, T. R., Jacob, D. J., Grossman, S., Lu, X., Qu, Z., Sulprizio, M. P., Zhang, Y., Reuland, F., Gordon, D., and Worden, J. R.: Updated Global Fuel Exploitation Inventory (GFEI) for Methane Emissions from the Oil, Gas, and Coal Sectors: Evaluation with Inversions of Atmospheric Methane Observations, Atmospheric Chemistry and Physics, 22, 3235–3249, https://doi.org/10.5194/acp-22-3235-2022, 2022.

Schuldt, K. N., Aalto, T., Aaltonen, H., Arlyn Andrews, Apadula, F., Arnold, S., Bäni, L., Bartyzel, J., Bergamaschi, P., Biermann, T., Biraud, S. C., Pierre-Eric Blanc, Brunner, D., Van Den Bulk, P., Francescopiero Calzolari, Huilin Chen, Lukasz Chmura, Coletta, J. D., Colomb, A., Condori, L., Conen, F., Conil, S., Couret, C., Cristofanelli, P., Cuevas, E., Delmotte, M., Ankur Desai, Elsasser, M., Emmenegger, L., Forster, G., Frumau, A., Fuente-Lastra, M., Galkowski, M., Francois Gheusi, Hammer, S., Haszpra, L., Hatakka, J., Heliasz, M., Heltai, D., Henne, S., Hensen, A., Hermans, C., Hermansen, O., Hoheisel, A., Holst, J., Di Iorio, T., Jaffe, D. A., Karion, A., Kazan, V., Keronen, P., Kneuer, T., Kolari, P., Kominkova, K., Kubistin, D., Kumps, N., Lan, X., Lanza, A., Laurent, O., Lee, J., Lehner, I., Lehtinen, K., Leskinen, A., Leuenberger, M., Levin, I., Levula, J., Lindauer, M., Lindroth, A., Mikaell Ottosson Löfvenius, Lopez, M., Lunder, C. R., Mammarella, I., Manca, G., Marek, M. V., Marklund, P., De Mazière, M., McKain, K., Meinhardt, F., Jean-Marc Metzger, Miller, C. E., Miller, J. B., Mölder, M., Müller-Williams, J., Myhre, C. L., Jaroslaw Necki, Noe, S. M., O'Doherty, S., Peltola, O., Philippon, C., Piacentino, S., Pichon, J. M., Pickers, P., Pitt, J., Plass-Dülmer, C., Platt, S. M., Ramonet, M., Louis-Jeremy Rigouleau, Rivas, P. P.,

Yves-Alain Roulet, Di Sarra, A. G., Scheeren, B., Schmidt, M., Schumacher, M., Sha, M. K., Sloop, C. D., Smith, P. D., Sørensen, L. L., Steger, D., Steinbacher, M., Sweeney, C., Taipale, R., Thoning, K., Trisolino, P., Vermeulen, A., Viner, B., Vitkova, G., Weyrauch, D., Worthy, D., Xueref-Remy, I., Yver-Kwok, C., and Miroslaw Zimnoch: Multi-Laboratory Compilation of Atmospheric Carbon Dioxide Data for the Year 2024; obspack_ch4_1_NRT_v7.1_2025-01-31, https://doi.org/10.25925/20250115, 2025.

Stavert, A. R., Saunois, M., Canadell, J. G., Poulter, B., Jackson, R. B., Regnier, P., Lauerwald, R., Raymond, P. A., Allen, G. H., Patra, P. K., Bergamaschi, P., Bousquet, P., Chandra, N., Ciais, P., Gustafson, A., Ishizawa, M., Ito, A., Kleinen, T., Maksyutov, S., McNorton, J., Melton, J. R., Müller, J., Niwa, Y., Peng, S., Riley, W. J., Segers, A., Tian, H., Tsuruta, A., Yin, Y., Zhang, Z., Zheng, B., and Zhuang, Q.: Regional Trends and Drivers of the Global Methane Budget, Global Change Biology, 28, 182–200, https://doi.org/10.1111/gcb.15901, 2022.

Tans, P. P.: A Note on Isotopic Ratios and the Global Atmospheric Methane Budget, Global Biogeochemical Cycles, 11, 77–81, https://doi.org/10.1029/96GB03940, 1997.

van Wees, D., van der Werf, G. R., Randerson, J. T., Rogers, B. M., Chen, Y., Veraverbeke, S., Giglio, L., and Morton, D. C.: Global Biomass Burning Fuel Consumption and Emissions at 500 m Spatial Resolution Based on the Global Fire Emissions Database (GFED), Geoscientific Model Development, 15, 8411–8437, https://doi.org/10.5194/gmd-15-8411-2022, 2022.

Weber, T., Wiseman, N. A., and Kock, A.: Global Ocean Methane Emissions Dominated by Shallow Coastal Waters, Nature Communications, 10, 4584, https://doi.org/10.1038/s41467-019-12541-7, 2019.